Sensors & Actuators: A. Physical 365 (2024) 114859

Contents lists available at ScienceDirect

Sensors and Actuators: A. Physical

journal homepage: www.journals.elsevier.com/sensors-and-actuators-a-physical

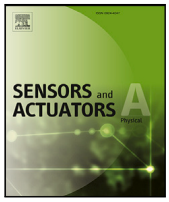

Simulation of electron transport and secondary emission in a photomultiplier tube and experimental validation

Pablo Martín-Luna [a,*], Daniel Esperante [a,b], Antonio Fernández Prieto [c], Nuria Fuster-Martínez [a], Iris García Rivas [c,d], Benito Gimeno [a], Damián Ginestar [e], Daniel González-Iglesias [a], José Luis Hueso [e], Gabriela Llosá [a], Pablo Martinez-Reviriego [a], Alba Meneses-Felipe [a,f], Jaime Riera [e], Pablo Vázquez Regueiro [c], Fernando Hueso-González [a]

[a] Instituto de Física Corpuscular (IFIC), CSIC–UV, c/ Catedrático José Beltrán 2, 46980 Paterna, Spain
[b] Electronics Engineering Department, Universitat de València, 46100 Burjassot, Spain
[c] Instituto Galego de Física de Altas Enerxías (IGFAE), Universidade de Santiago de Compostela, Santiago de Compostela, Spain
[d] Triple Alpha Innovation SL, La Coruña, Spain
[e] Instituto de Matemática Multidisciplinar, Universitat Politècnica de València, Camí de Vera, s/n, 46022 València, Spain
[f] Grupo de Física Médica y Biofísica, Universidad de Navarra, 31008 Pamplona, Spain

ARTICLE INFO

Keywords:
Photomultiplier tube
Photodetector
Proton therapy
Monte Carlo simulation
Measurement

ABSTRACT

The electron amplification and transport within a photomultiplier tube (PMT) has been investigated by developing an in-house Monte Carlo simulation code. The secondary electron emission in the dynodes is implemented via an effective electron model and the Modified Vaughan's model, whereas the transport is computed with the Boris leapfrog algorithm. The PMT gain, rise time and transit time have been studied as a function of supply voltage and external magnetostatic field. A good agreement with experimental measurements using a Hamamatsu R13408-100 PMT was obtained. The simulations have been conducted following different treatments of the underlying geometry: three-dimensional, two-dimensional and intermediate (2.5D). The validity of these approaches is compared. The developed framework will help in understanding the behavior of PMTs under highly intense and irregular illumination or varying external magnetic fields, as in the case of prompt gamma-ray measurements during pencil-beam proton therapy; and aid in optimizing the design of voltage dividers with behavioral circuit models.

1. Introduction

The invention of the PMT, a device capable of detecting down to one single photon and generating an amplified electrical signal of it, dates back to almost a century ago [1,2]. Since then, its use has grown dramatically and its deployment pervades today a myriad of fields such as homeland security, nuclear physics, life sciences, medical imaging [3] as well as treatment monitoring [4,5].

Throughout the last century, PMTs have been thoroughly studied from theoretical, semi-empirical and statistical points of view [2,6,7], and many PMT models from diverse vendors were experimentally characterized in the literature. Likewise, behavioral circuit models [8–10] were deployed to optimize the voltage supply electronics [11]. Their robustness against radiation damage [12] and quickly changing count rates [13] is actively investigated.

In spite of the abundant literature, we found that its behavior is not yet fully understood based on fundamental physics principles. For example, the space-charge effect [3,14] (where a densely packed electron cloud perturbs the accelerating electric field) is known to disturb the gain linearity [15,16] with high illumination. Likewise, the Earth's or any external magnetic field influence the PMT gain and signal shape. However, there is a trend to explain these phenomena from a qualitative or empirical point of view, with only recent simulations of the effect of magnetic field on a microchannel plate detector [17].

To cover the gap, we have developed a framework to perform Monte Carlo (MC) simulations of the electron cascade within the vacuum of a PMT, as done also by [18]. On the one hand, the goal is to calculate basic PMT traits such as gain, rise time and transit time as function of supply voltage and external magnetostatic field, and to validate it with experimental measurements. On the other hand, we aim at establishing a solid, fast and generic simulation tool, so that it can be used in the future for:

* Corresponding author.
E-mail addresses: pablo.martin@uv.es (P. Martín-Luna), fernando.hueso@uv.es (F. Hueso-González).

https://doi.org/10.1016/j.sna.2023.114859
Received 20 June 2023; Received in revised form 9 November 2023; Accepted 21 November 2023
Available online 30 November 2023

Abbreviations

The following abbreviations are used in this manuscript:

CT	Computed Tomography
LED	Light-Emitting Diode
FWHM	Full Width at Half Maximum
MC	Monte Carlo
PMT	Photomultiplier Tube
SPICE	Simulation Program with Integrated Circuit Emphasis
SVG	Scalable Vector Graphics
SEY	Secondary Electron Yield
STL	STereoLithography

- linking it to a Simulation Program with Integrated Circuit Emphasis (SPICE) [19] that optimizes the voltage divider [8] taking into account the dynode collection efficiency as well as the ripple of the high voltage supply,
- predicting the onset of space charge with high illumination conditions during short pulses, and
- studying the effect of rapidly changing external magnetic fields on the PMT gain and on the shielding efficiency.

In particular, these conditions appear in the field of prompt γ-ray measurements during proton therapy treatments: changing magnetic fields are produced for pencil-beam scanning and extremely high count rates reach uncollimated γ-ray detectors [20], especially in the case of detectors located coaxial to the beam and close to the irradiated area [21].

The manuscript is organized as follows. In Section 2, we describe the framework for the MC simulation of the electron cascade, namely the underlying physical processes 2.1 and the geometrical model on which Poisson's equation is solved 2.2. In Section 3, we compare the simulation results with experimental measurements to validate the developed platform. In Section 4, we discuss the main findings and summarize the future research lines.

2. Simulation program

The simulation of the amplification and transport of electrons in a realistic PMT geometry is carried out by means of an in-house developed code based on the tracking of an electron within the device, whose motion is governed by the electrostatic field, cf. Section 2.1.

The underlying geometry, cf. Section 2.2, mimicks the 8-dynode linear-focused ⌀1.5" R13408-100 PMT from Hamamatsu (Hamamatsu, Japan), as shown in Fig. 1. The recommended electrode voltages are displayed in Table 1.

2.1. General considerations

The overview of the simulation code is represented in a flowchart in Fig. 2. It includes the emission of electrons in a PMT, electron transport, emission of secondary electrons and collection in the anode grid.

2.1.1. Emission

The emission of electrons in a PMT is produced in a photocathode that is located just behind a window (lens) that focuses incoming light. The photocathode is a semitransparent thin layer with a photoemissive material deposited on the inner surface of the window. It absorbs the optical photons and emits photoelectrons (with a certain probability or quantum efficiency, depending on the wavelength) because of the photoelectric effect. In our code, it is assumed that electrons are uniformly emitted from the surface of the photocathode without kinetic energy.

2.1.2. Transport

The electron movement in a PMT is mainly affected by the electrostatic field, which depends on the electrode configuration and the voltage applied to each electrode. Consequently, the electron trajectories are determined by finding the potential distribution and solving the equation for motion: the Lorentz force. The electrostatic field can be calculated at the particle positions by means of an interpolation between mesh points (cf. Section 2.2). Then, the non-relativistic Lorentz force acting on each particle is determined and the differential equation of motion is solved numerically for each electron by means of a *leapfrog* algorithm, specifically the Boris method [22,23] with time steps of 8 ps and neglecting space-charge effects. This procedure allows us to update the electron position and velocity within the PMT.

2.1.3. Secondary emission

The electrons are multiplied within the PMT when they impact on several electrodes (dynodes) that are covered with a layer of secondary emissive material. Thus, for each incident electron, each dynode emits a certain number of secondary electrons. As a consequence, after each position update it is checked if the particle collides with any electrode. When such an event occurs, the interaction between the electron and the metal surface is modeled by calculating the total SEY coefficient δ of the material that is the average number of electrons emitted per incident one. The SEY coefficient has been computed using the Modified Vaughan's model [24,25] in which the SEY curve $\delta(E,\theta)$ as a function of the impacting electron kinetic energy E and the incident angle θ respect to the surface normal is given by

$$\delta(E,\theta) = \begin{cases} \delta_{\text{low}} & \text{for} \quad v(E) < 0, \\ \delta_{\max}(\theta)\left(ve^{1-v}\right)^{\alpha} & \text{for} \quad 0 \le v(E) \le 3.6, \\ \delta_{\max}(\theta)\frac{1.125}{v^{0.35}} & \text{for} \quad v(E) > 3.6, \end{cases} \tag{1}$$

$$v(E) = \frac{E - E_0}{E_{\max}(\theta) - E_0}, \tag{2}$$

$$\delta_{\max}(\theta) = \delta_{\max}\left(1 + k_\delta \theta^2/(2\pi)\right), \tag{3}$$

$$E_{\max}(\theta) = E_{\max}\left(1 + k_E \theta^2/(2\pi)\right), \tag{4}$$

where $v(E)$ is a dimensionless parameter, $\delta_{\text{low}} \in [0,1]$ is the SEY value at low impacting energies (typically close to the unity, because at these energies electrons are mainly reflected on the surface), E_0 is a parameter related to the work function, k_δ and k_E are factors related to the roughness of the surface, (normally close to 1), $\delta_{\max}(E_{\max})$ is the maximum SEY value, and α is a material-dependent fit parameter. In the simulations, we will consider that the dynodes 3, 4 and 5 are made of CuBeO and the rest of dynodes of Cs_3Sb. The SEY curves of these materials are shown in Fig. 3 and have been fitted to the Modified Vaughan's model based on the SEY curves (for normal incidence) shown in [3,26]. It can be seen that the SPICE behavioral models use a simplification ($\delta = rE^{\beta}$) that does not reproduce the shape of actual SEY curves.

Although the number of electrons emitted from the surface after a collision should be calculated using a Poisson or Polya [7] distribution with mean δ, it has been checked that the results do not change if it is assumed that an exact number δ of electrons are released each time. This amplification is modeled considering one effective electron (with mass $M = Nm_e$ and charge $Q = -Ne$; m_e and $-e$ are the rest mass and charge of the electron), which represents a number N of real electrons. The effective electron has the same charge-to-mass ratio as a single one, and consequently the dynamics of the effective electron is the same as that of an individual one. Hence, after J impacts, the number of electrons associated to the effective electron is

$$N = \prod_{j=1}^{J} \delta_j, \tag{5}$$

where δ_j is the SEY value corresponding to the jth collision. If the impacting kinetic energy E_j is lower than E_0 we consider that the

Table 1
Recommended voltage ratios between cathode, grid, dynodes, Acc and anode of the ⌀1.5" R13408-100 PMT.

Electrodes	Cathode	Grid	Dy1	Dy2	Dy3	Dy4	Dy5	Dy6	Dy7	Dy8 (Acc)	Anode
Ratio	1.3		4.8	1.5	1.5	1	1	1	1	1	1

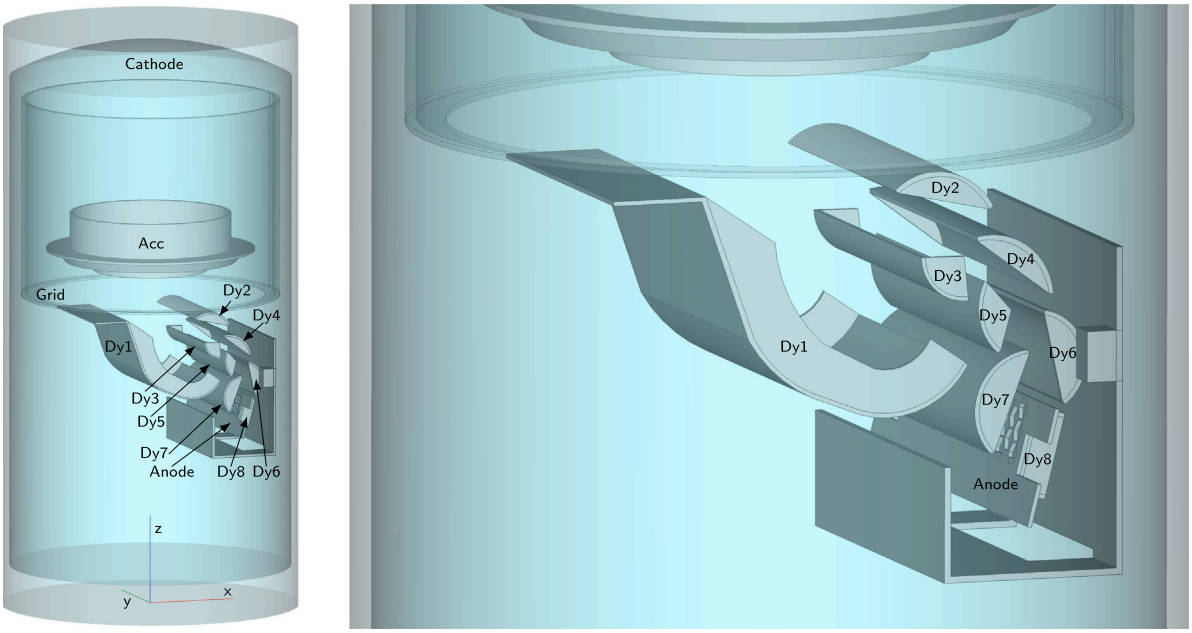

Fig. 1. Illustration of the PMT structure (detail of the dynode geometry on the right), as designed in FreeCAD. Note the cylindrical symmetry of the focusing electrode or grid and the acceleration electrode (Acc).

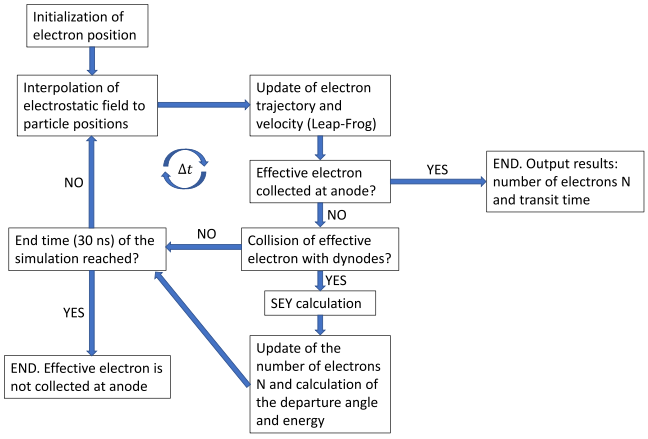

Fig. 2. Simulation code flowchart for each electron emitted from the cathode.

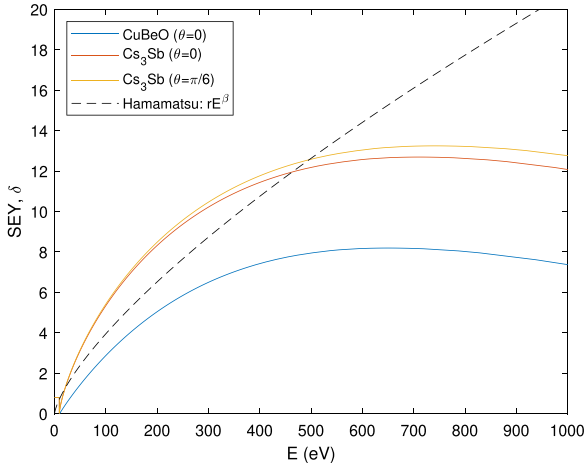

Fig. 3. Simulated SEY curves using the Modified Vaughan's model with $\delta_{\text{low}} = 0.8, k_E = 1, k_\delta = 1, E_0 = 10\,\text{eV}$, $E_{\text{max}} = 650\,\text{eV}$, $\delta_{\text{max}} = 8.2$ and $\alpha = 0.95$ for CuBeO and $\delta_{\text{low}} = 0.8, k_E = 1, k_\delta = 1, E_0 = 9.15\,\text{eV}$, $E_{\text{max}} = 710\,\text{eV}$, $\delta_{\text{max}} = 12.7$ and $\alpha = 0.7377$ for Cs_3Sb. The parameters for the curve derived from the Hamamatsu datasheet are $r = 0.1423, \beta = 0.7219$. The value of k_δ will be fitted in Section 3.2.

effective electron is elastically reflected in the surface (i.e. with the same energy and angle relative to the surface as on impact) with $\delta_j = \delta_{\text{low}}$. Otherwise, if $E > E_0$, the departure energy E_{out} is calculated using a Rayleigh distribution [27]:

$$E_{\text{out}} = \sigma_{\text{E}} \sqrt{-2 \ln u_1}, \tag{6}$$

where $u_1 \in [0, 1]$ is a random number and σ_{E} is an empirical parameter, typically in the range of a few eV that is fitted to the experimental results. The direction of emission will be explained in Section 2.2, since it depends on the chosen geometrical model.

2.1.4. Collection

In a PMT the electron avalanche is collected in an anode grid providing an output signal. Nevertheless, as we use an effective model in our simulations we obtain the time that the nth original emitted electron takes to arrive to the anode and the number of electrons N_n that it represents. A total of $N_{\text{T}} = 50\,000$ electrons are emitted (uniformly distributed) from the photocathode; the Gain is given by

$$\text{Gain} = \frac{\sum_{n=1}^{K} N_n}{N_{\text{T}}}, \tag{7}$$

where $K \leq N_{\text{T}}$ is the number of effective electrons that are collected in the anode. There are some electrons that are lost in the aperture between dynodes or have a huge number of impacts at lower energies ($E < E_0$) with $\delta < 1$. For this reason, if a maximum simulation time

of 30 ns is reached we assume that the effective electron will not be collected at the anode. The temporal figures of merit of the PMT are obtained by fitting a Gaussian curve to the histogram of the number of collected electrons as a function of transit time (cf. Fig. 7).

2.2. Geometry

In order to obtain a detailed internal image of the PMT, a Computed Tomography (CT) with a reconstructed voxel size of 50 μm × 50 μm × 200 μm has been acquired with a NAEOTOM Alpha scanner of Siemens Healthineers (Forchheim, Germany). The software 3D Slicer [28] was used to contour each electrode. Further high-resolution X-ray images were acquired with the small-animal SuperArgus PET/CT 4r scanner of Sedecal (Algete, España), with a panel pixel size of 75 μm × 75 μm. In this case, the reconstruction was performed using an in-house code based on the Reconstruction Toolkit (RTK) [29] and independently verified via MATLAB's inverse radon transform (out of the Image Processing Toolbox) [30] by MathWorks (version 2022b). Information from both CT scans as well as direct measurements with a calliper were then combined to retrace the PMT geometry in a simplified parametric manner (with an estimated uncertainty of 0.3 mm), deploying the 3D computer-aided design modeler FreeCAD [31], cf. Fig. 1. Finally, the 3D geometry was exported as separate files in STereoLithography (STL) format for each electrode.

To perform the simulations, we have followed three different strategies (3D, 2D and 2.5D) based on the original 3D geometry, and their differences are described below. An animated simulation of the electron transport is included in the supplementary materials (Fig. S1).

2.2.1. 3D strategy

A quadratic tetrahedral mesh was defined in MATLAB using as underlying geometry the imported STL file triangles. The electrostatic field is computed in the mesh by solving Poisson's equation (Dirichlet boundary conditions applied on the electrodes' surface at their supplied voltage) with MATLAB's Partial Differential Equation Toolbox [30] by MathWorks (version 2022b), which is based on finite element analysis. It is important to remark that the mesh triangles near the anode region have to be extremely fine: a value equal or smaller than 0.2 mm for parameter `Hface` (mesh target size on selected faces) is needed; for the remaining 3D geometry a value of 2 mm of the parameter `Hmax` (upper bound on the mesh edge lengths) is sufficient.

At each time step it is checked if the particle collides with the 3D geometry of any electrode via Tuszynski's `in_polyhedron` function [32]. The direction of the emitted secondary electrons is obtained assuming a local spherical coordinate system centered at the impact point of the electron and calculating the polar angle (respect to the normal of the surface) and azimuthal angle using the 3D cosine law [33] and a uniform probability density, respectively

$$\theta_{\text{out}} = \arcsin(\sqrt{u_2}), \tag{8}$$

$$\varphi_{\text{out}} = 2\pi u_3, \tag{9}$$

where $u_i \in [0, 1]$ are random numbers.

2.2.2. 2D strategy

In this case, the 3D PMT geometry of the STL was reduced to a 2D geometry by calculating its intersection with the plane $y = 0$ (cf. Fig. 4(b)). Here, the Poisson Superfish software [34], which is a code capable of solving 2D electrostatic geometries quickly is used to calculate the electrostatic fields. As the trajectories of the effective electrons are confined in the plane $y = 0$, the transport and amplification algorithm comprises the following differences with respect to the 3D strategy:

- Electrons are emitted from the cathode, which in this model is an arc line.
- The 3D cosine law is changed by the 2D cosine law [33]:

$$\theta_{\text{out}} = \arcsin(u_2), \tag{10}$$

The angle θ_{out} is chosen clockwise or counterclockwise randomly with respect to the normal, and φ_{out} is not computed.

Table 2
Time of computation required to calculate the electrostatic fields (Poisson's equation) and to run each simulation (electron transport and amplification) of the $N_T = 50\,000$ emitted electrons, at a supply voltage of $U = -1500$ V. Note that the time reported in the "Electron simulation" column is roughly proportional to the electron transit time: at $U = -700$ V, these values almost double. The simulations were performed employing a standard desktop computer (Intel Core i7-6700 K, 4.00 GHz, 16-GB RAM).

Strategy	Field calculation	Electron simulation	Total simulation
2D	~1 min	~1 h	~1 h
2.5D	~1 min	~1 h	~1 h
3D	~4 h	~3 h	~7 h

2.2.3. 2.5D strategy

This case also calculates the intersection of the 3D geometry with the plane $y = 0$, but extrudes the resulting projection infinitely in y. In other words, it is assumed that the 2D geometry is invariant in the perpendicular direction to the 2D plane. Therefore, this resembles the 2D strategy: the electrostatic field solution is that of the 2D model, with the difference that electrons can move in 3D. Only the coordinates (x, z) of the electron's position are used to evaluate the electrostatic field and for checking if the electron impacts on an electrode. In order to allow the movement in 3D, the direction of emission of the electrons is calculated as in the 3D strategy given by Eqs. (8)–(9). It is worth noting that the emission points on the photocathode are sampled randomly along an arc contained in the plane $y = 0$. Hence, the coordinate y of the electron can only vary (move in 3D) after bouncing on the first dynode.

The main advantage of the 2D and 2.5D strategies is the simplicity of a 2D geometry compared to the real 3D geometry. Consequently, the algorithms are simpler to implement and the simulations are much faster (see Table 2), especially while solving Poisson's equation and identifying the impact on an electrode. In the following section, we will compare the obtained results using the three strategies and we will study under what conditions the simulations using the complete 3D model can be approximated by the 2D or 2.5D strategies.

Note that, in Sections 3.2 and 3.4, the parameters σ_{E}, k_δ and the external magnetostatic field $\vec{B}$, just affect the electron transport and amplification equations. They do not change the electrostatic field solution; hence, to increase the total simulation speed, the calculated fields will be calculated once, stored, and reloaded each time a parameter is changed.

3. Results

3.1. Electrostatic fields

Firstly, the electrostatic field solution obtained using the 3D and 2D strategies are compared. Fig. 4(a) shows the equipotential lines in the plane $y = 0$ if the electrostatic problem is solved with MATLAB using the 3D geometry and Fig. 4(b) shows the equipotential lines if the electrostatic problem is solved with Poisson Superfish using the 2D geometry. (We also calculated it in 2D with MATLAB, with negligible differences (always smaller than 1 V) compared to Superfish, checking that both Poisson's equation solvers are compatible.) On the one hand, it can be seen that the main differences between 3D and 2D (cf. Fig. 4(c)) are produced in the region between the cathode and the first dynode because the cathode, grid and Acc have cylindrical geometry that cannot be properly taken into account in the 2D projection. This oversimplification causes the electrons emitted from the cathode to reach the first dynode earlier in time, cf. Figs. 5(a) and S2. On the

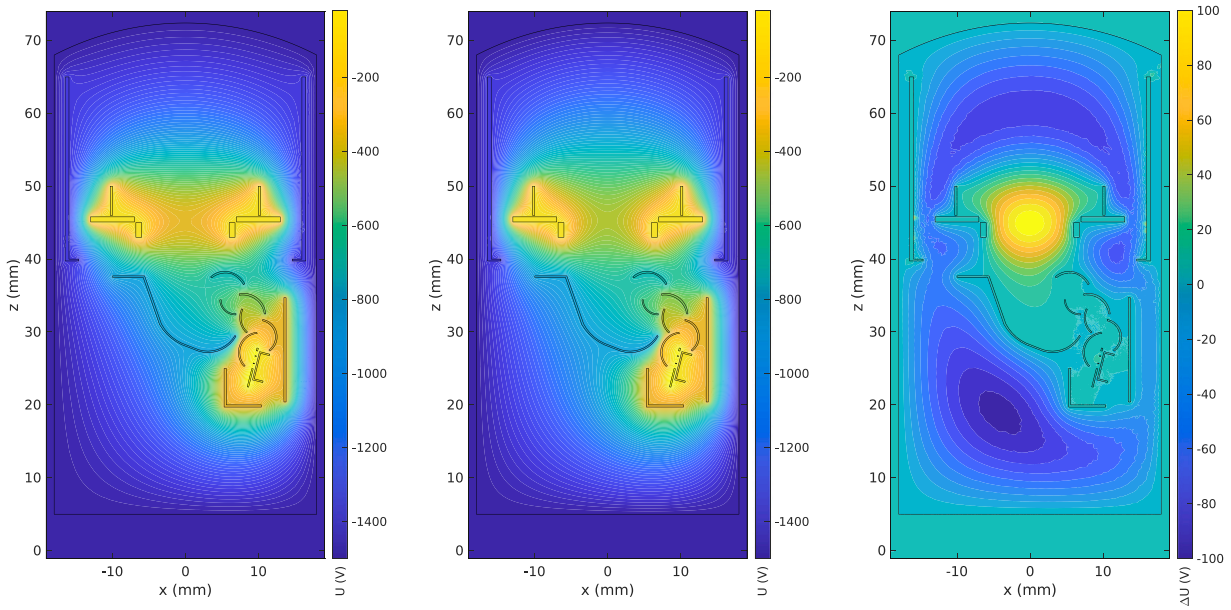

(a) 3D geometry (b) 2D geometry (c) Difference 3D − 2D

Fig. 4. Equipotential lines of the electrostatic solution at the plane $y = 0$ for a supply voltage of −1500 V. The 2D cross section of the electrodes is shown in black. Equipotential steps of 20 V (3D, 2D) and 10 V (difference) are shown in white.

other hand, the difference in the electrostatic potential in the dynodes' region is rather small: $\lesssim$0.5 V between Dy2 and Dy6, and $\lesssim$15 V near the anode: here the electron trajectories will be comparable.

3.2. Optimized parameters

We have described before two free parameters of the physics model: k_δ that is close to the unity and is related to the angular dependence of the SEY; and σ_E that is typically of a few eV and is related to the energy of the emitted electrons. These parameters can be finely adjusted in order to fit the simulation results to the reference datasheet of the PMT: an electron transit time of 13 ns and a gain of 3.8×10^5 for a supply voltage U of −1500 V. Fig. 5 shows the electron transit time and gain as a function of σ_E for $k_\delta = 1$. Thus, to fit the transit time in the 3D strategy, the optimal value is $\sigma_E = 2.2$ eV, and to fit the gain it can be seen that the other optimal value is $k_\delta = 1.11$ and $k_\delta = 1.28$ (both for CuBeo and Cs_3Sb) for the 3D and 2.5D strategies, respectively. The optimal value for k_δ for the 2D approach is too high to be physically possible, so we will take a value of $k_\delta = 1$ for future plots.

Hence, these simulations serve as a comparison of the strategies presented. It can be seen that the 2D approach underestimates the gain compared to the 2.5D and 3D strategies. This is mainly due to two factors: (i) the 2D cosine law provides larger angles with respect to the surface normal compared to 3D cosine law, which means that more electrons are lost between the slits of the dynodes; and (ii) the impacting angle with respect to the normal of the dynodes is smaller by not taking into account the 3D trajectory of the electrons. Therefore, the 2D strategy is not a good approximation to simulate the amplification of electrons in a PMT. Note that the discrepancy in the gain between the 2.5D and 3D approaches is not too high: lower than 10% if the same value of k_δ is used in both strategies. On the other hand, it can be seen that the 2D and 2.5D strategies underestimate the transit time compared to the 3D approach. As previously mentioned, this discrepancy is basically due to the difference between 3D and 2D electrostatic fields in the area from the cathode to the first dynode.

3.3. Effect of supply voltage

We studied the PMT gain and the temporal magnitudes as a function of the supply voltage for the different strategies using the optimized parameters, and compare it with experimental measurements using an HVLAB3000 from ET Enterprises (Uxbridge, UK) as negative high voltage supply (1 V nominal precision). The DC–coupled voltage divider was manufactured by IGFAE following the standard ratios (cf. Table 1). The anode signal was digitized with an 8-bit 2.5 GHz WaveRunner 625Zi oscilloscope operated at sampling rates between 2.5 and 40 Gsps, and the raw waveforms were processed off-line. Each data acquisition consisted of at least 10 000 waveforms to minimize the statistical error; the experimental uncertainty was thus dominated by systematic factors like the empirical calibration of the PMT gain and the electron transit time at a fixed voltage, as well as the electronic noise when measuring at very low tube voltages (PMT gains). Some measurements were performed with the bare PMT inside a dark box or in front of a pulsed LED [35], whereas other measurements were performed with the PMT optically coupled to a $CeBr_3$ monolithic scintillation crystal (⌀1"×1"). The uncertainties in the simulations are equally dominated by systematic effects, such as the contouring of the dynode geometry and the finite element mesh size.

As it can be seen in Fig. 6(a), the gains obtained in the simulations with the 2.5D and 3D strategies are in good agreement with the experimental measurements, although there is a discrepancy at lower voltages because the SEY curve of the materials is probably underestimated with respect to the real one. The relative gain deviation between the 2.5D or 3D strategy and the reference values from the Hamamatsu datasheet is smaller than 10% within the range $U \in [-1750, -1000]$ V. Besides, the non-linearity in the experimental gain at higher voltages cannot be explained with the simulations since it stems from variations in the dynodes' voltages due to the currents flowing into the passive divider network of the PMT supply [8]. As previously discussed, the 2D approach is not a good approximation in order to simulate the amplification of electrons in the PMT.

On the other hand, the electron transit time as a function of the voltage (Fig. 6(b)) is satisfactorily described with the simulations, although the 2D and 2.5D strategies underestimate it (a 3%–4% compared to the 3D strategy). Furthermore, the rise time (10%–90%) as a function of the supply voltage (Fig. 6(c)) calculated using the 3D approach is in very good agreement (within 8% over the whole range) with the experimental measurements with dark counts, whereas the 2D and 2.5D strategies overestimate the rise time (by minimum 3% and

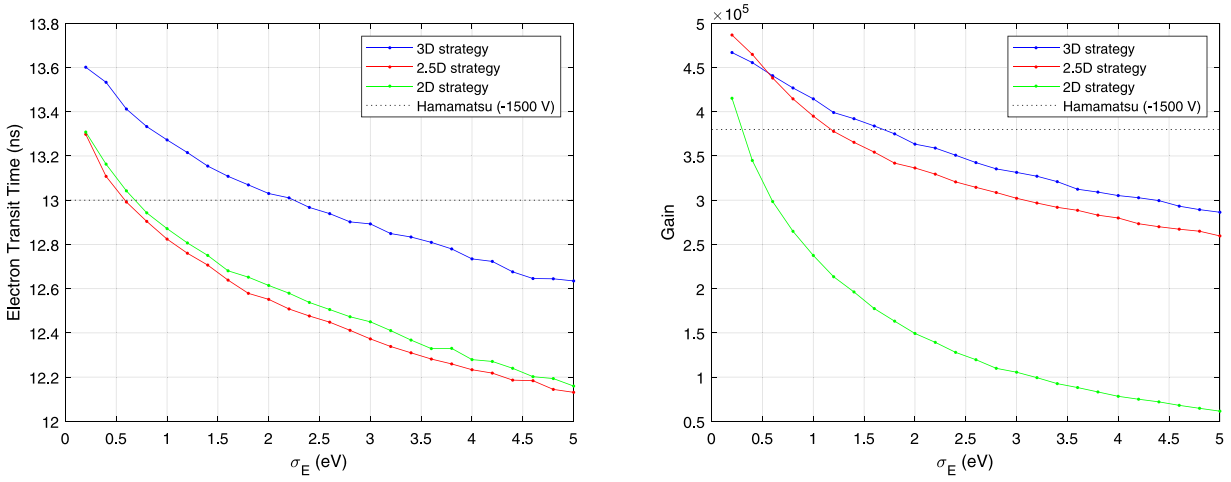

(a) Electron transit time (b) Gain

Fig. 5. PMT traits as a function of the parameter σ_E for the 3D, 2.5D and 2D strategies at a supply voltage U of −1500 V and $k_\delta = 1$.

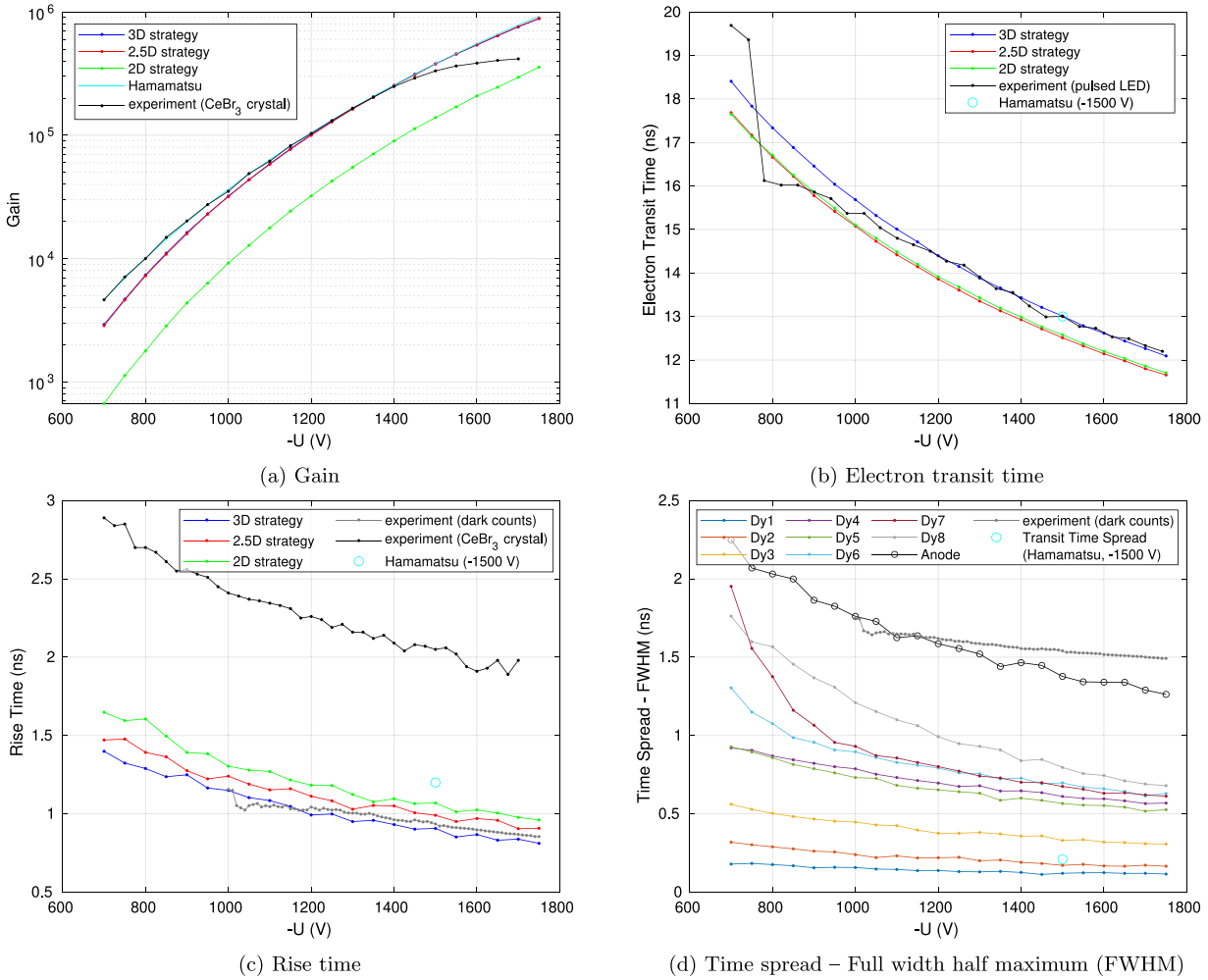

(a) Gain (b) Electron transit time

(c) Rise time (d) Time spread – Full width half maximum (FWHM)

Fig. 6. PMT traits as a function of the supply voltage U for the optimized parameters $\sigma_E = 2.2$ eV and $k_\delta = 1.11$ (3D), $k_\delta = 1.28$ (2.5D), $k_\delta = 1$ (2D, not optimal) for the 3D, 2.5D and 2D strategies compared with experimental measurements (PMT in darkness or in front of a pulsed LED [35], or coupled with a $CeBr_3$ crystal and in front of a ^{22}Na source). Fig. 6(d) shows the results only for the 3D strategy; the FWHM for Dy8 is obtained by a Gaussian fit of the first peak in the time spread pulse (cf. Fig. S2).

maximum 27%). Similar percentage errors in these figures of merit are obtained in [18] with a completely independent code (based on an individual electron model and using COMSOL Multiphysics® [36] instead of an effective electron model and MATLAB/Superfish) and PMT models (from ET Enterprises instead of Hamamatsu). It can be seen that the simulated values underestimate the rise time compared to the experimental measurements with a $CeBr_3$ crystal although they follow a similar trend. This result most probably stems from the spread of scintillation photons inside the crystal. In the measurements with dark counts (no crystal, no ^{22}Na source), this effect is absent, which explains their better agreement with the simulations.

Fig. 6(d) depicts the time spread of the pulses collected at each dynode and the anode using the 3D strategy, showing that, in general, these pulses broaden as electrons move from one dynode to the next. The FWHM of the anode pulse as a function of the supply voltage is in good agreement (within 15% over the whole range) with the experimental measurements with dark counts. The 2D and 2.5D strategies provide slightly larger values than the 3D strategy (cf. Fig. S2), similarly to the trend in the rise time. It is worth noting that Fig. 6(d) can be employed to estimate the jitter in the transit time. Actually, the jitter stems from statistical fluctuations of the paths described by the electrons that are produced when there is still a small number of real electrons within the PMT. Thus, the major contribution to the jitter in the electron transit time arises from the different trajectories that electrons follow from the cathode to the first dynode [2], but also from the first dynode to the second (since the distance between these dynodes is also large in the studied PMT, cf. Fig. 1). Therefore, the jitter in the transit time may be estimated as the FWHM of the collected pulse at the second dynode. Fig. 6(d) shows that the jitter (FWHM) in the transit time given by the manufacturer (210 ps at $U = -1500$ V) agrees well with the FWHM of the pulse at the second dynode. The simulated value is probably underestimating the real value because of the small contribution to the jitter in the transit time due to the electron transport from the second to the following dynodes.

For completeness, Fig. 7 shows some examples of the histograms of the number of electrons collected in the anode as a function of the transit time that we obtain in the simulations performed with the 3D strategy. They are compared to the corresponding experimental measurements (with dark counts). The oscillations after the main pulse are an artifact due to the measurement electronics.

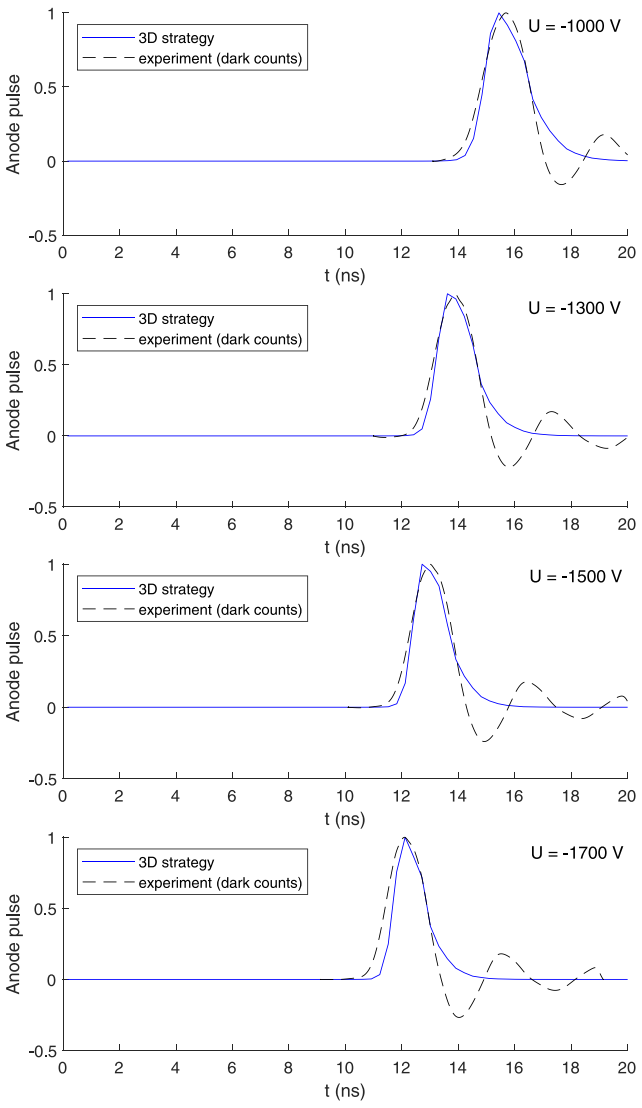

Fig. 7. Comparison between the simulated (3D strategy, with the optimized parameters $\sigma_E = 2.2$ eV and $k_\delta = 1.11$) and experimental signal shape (normalized to the unity) at the anode for different supply voltages. The simulated signal shape has been obtained using $N_T = 300\,000$ (N_T is increased to obtain a smoother pulse) photoelectrons emitted from any part of the cathode simultaneously at $t = 0$, whereas the experimental signal shape is an average of 10 000 pulses. The experimental signal shape has been horizontally shifted based on the simulated transit time (cf. Fig. 6(b)).

3.4. Effect of an external magnetostatic field

Finally, the effect of an external magnetostatic field $\vec{B}$ in the operation of the PMT is studied, assuming that no magnetic shield is deployed around it. Fig. 8 shows the variation of the gain in the presence of an external magnetic field in the three directions of space. Results are qualitatively similar to the vendor's reference data: the effect of a magnetostatic field on the y-axis is most critical and less important on the z-axis. On the other hand, the results obtained with the 3D strategy are the most similar to the ones provided by Hamamatsu, although the differences with the other approaches are not too marked.

4. Conclusions

In this work, the transport and amplification of electrons in a PMT has been studied by means of numerical simulations performed with an in-house developed code (in MATLAB) obtaining a good agreement with experimental measurements. Three different strategies have been implemented and compared. The 3D strategy provides the best results compared to the experimental measurements since it is the only approach that takes into account the 3D geometry of the PMT, whereas the 2D strategy is not sufficient to describe the amplification of the electrons. Nevertheless, the 2.5D approach is a good approximation for studying the gain in the absence of an external magnetic field, with a much lower computational cost.

The conducted simulations cannot explain the non-linearity at higher voltages observed experimentally, whose reason is the instability of the dynodes' voltages due to the currents flowing through the passive divider network of the PMT high voltage supply [8]. For this reason, the integration of the electromagnetic MC simulations with behavioral circuit simulation is foreseen. In this sense, the 2.5D strategy is postulated as a good candidate to perform these hybrid simulations including iterations. In the future, for fully emulating γ-ray detectors coupled with fast PMTs, we plan to convolve the result of the electromagnetic simulation with the optical MC simulation of photon transport in monolithic scintillation crystals. Furthermore, when deploying these detectors in prompt γ-ray based range verification in proton therapy, very high count rates in short bursts and changing magnetic fields are expected, and the incorporation of the space-charge and transient magnetic fields into the electromagnetic simulation will be necessary.

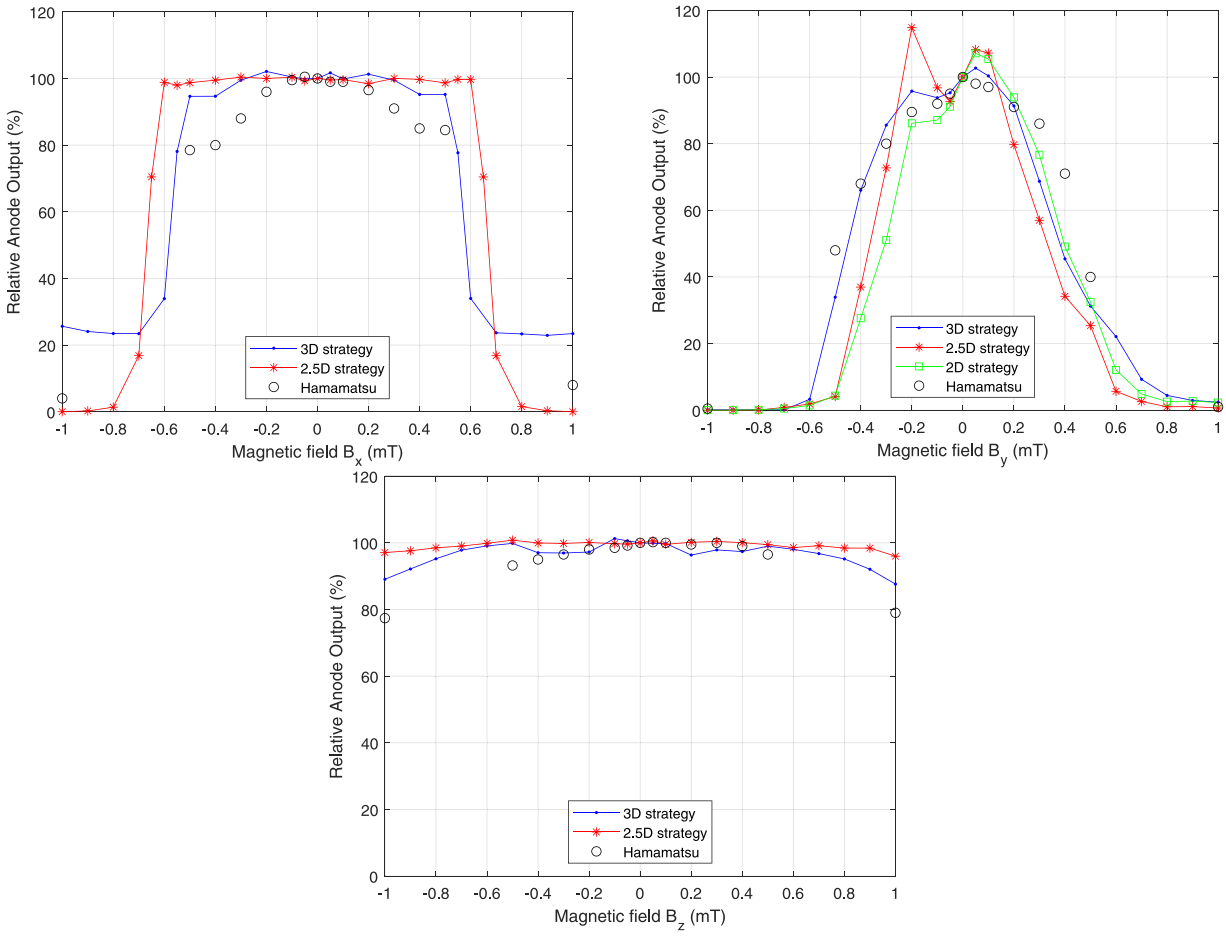

Fig. 8. Relative PMT gain without magnetic shield (normalized to the gain in absence of magnetic field) as a function of an external magnetostatic field for a supply voltage U of −1500 V and the optimized parameters $\sigma_E = 2.2$ eV and $k_\delta = 1.11$ (3D), $k_\delta = 1.28$ (2.5D), $k_\delta = 1$ (2D, not optimal). The results obtained with the different simulation strategies are compared with the experimental data provided by Hamamatsu.

CRediT authorship contribution statement

Pablo Martín-Luna: Conceptualization, Data curation, Formal analysis, Investigation, Methodology, Software, Validation, Writing – original draft, Writing – review & editing. **Daniel Esperante:** Supervision, Conceptualization, Methodology, Writing – review & editing. **Antonio Fernández Prieto:** Resources, Writing – review & editing. **Nuria Fuster-Martínez:** Funding acquisition, Supervision, Writing – review & editing. **Iris García Rivas:** Resources, Writing – review & editing. **Benito Gimeno:** Conceptualization, Methodology, Supervision, Writing – review & editing. **Damián Ginestar:** Software, Methodology, Writing – review & editing. **Daniel González-Iglesias:** Conceptualization, Software, Supervision, Writing – review & editing. **José Luis Hueso:** Software, Methodology, Writing – review & editing. **Gabriela Llosá:** Supervision, Funding acquisition, Writing – review & editing. **Pablo Martinez-Reviriego:** Supervision, Writing – review & editing. **Alba Meneses-Felipe:** Data curation, Writing – review & editing. **Jaime Riera:** Software, Methodology, Writing – review & editing. **Pablo Vázquez Regueiro:** Resources, Supervision, Writing – review & editing. **Fernando Hueso-González:** Conceptualization, Data curation, Funding acquisition, Investigation, Methodology, Software, Validation, Writing – original draft, Writing – review & editing.

Declaration of competing interest

The authors declare that they have no known competing financial interests or personal relationships that could have appeared to influence the work reported in this paper.

Data availability

Data will be made available on request.

Acknowledgments

This work was supported by Conselleria de Educación, Investigación, Cultura y Deporte (Generalitat Valenciana) under grant numbers CDEIGENT/2019/011 and CDEIGENT/2021/012. P. Martín-Luna is supported by the Ministerio de Universidades (Gobierno de España), Spain under Grant Number FPU20/04958. We thank Hamamatsu (V. Sánchez, D. Castrillo) for technical support and guidance; R. Carrasco (IFIC) and P. Wohlfahrt (Siemens Healthineers) for the CT scanning; D. Calvo and D. Real (KM3net-IFIC) for their LED test platform, the electronics and maintenance services at IFIC for excellent support; and K. Albiol, J. V. Casaña-Copado, A. Gallas Torreira, E. Lemos Cid, G. Pausch, A. Pazos Álvarez, E. Pérez Trigo, S. Rit, A. Ros, J. Roser, J. Stein, J. L. Taín and R. Viegas for useful discussions.

Appendix A. Supplementary data

Supplementary material related to this article can be found online at https://doi.org/10.1016/j.sna.2023.114859.

References

[1] B. Lubsandorzhiev, On the history of photomultiplier tube invention, Nucl. Instr. Methods Phys. Res. A 567 (1) (2006) 236–238, http://dx.doi.org/10.1016/j.nima.2006.05.221.

[2] A.G. Wright, The Photomultiplier Handbook, Oxford University Press, 2017, http://dx.doi.org/10.1093/oso/9780199565092.001.0001.
[3] K.K. Hamamatsu Photonics, Photomultiplier Tubes. Basics Ans Applications, fourth ed., 2017, URL https://www.hamamatsu.com/resources/pdf/etd/PMT_handbook_v4E.pdf.
[4] T. Werner, J. Berthold, F. Hueso-González, J. Petzoldt, K. Roemer, C. Richter, A. Rinscheid, A. Straessner, W. Enghardt, G. Pausch, Processing of prompt gamma-ray timing data for proton range measurements at a clinical beam delivery, Phys. Med. Biol. 1 (10) (2019) 105023, http://dx.doi.org/10.1088/1361-6560/ab176d.
[5] F. Hueso-González, M. Rabe, T.A. Ruggieri, T. Bortfeld, J.M. Verburg, A full-scale clinical prototype for proton range verification using prompt gamma-ray spectroscopy, Phys. Med. Biol. 63 (18) (2018) 185019, http://dx.doi.org/10.1088/1361-6560/aad513.
[6] S.O. Flyckt, C. Marmonier, Photomultiplier Tubes: Principles and Applications, second ed., Photonis, Brive-la-Gaillarde, France, 2002, URL https://www2.pv.infn.it/~debari/doc/Flyckt_Marmonier.pdf.
[7] G. Lachs, The statistics for the detection of light by nonideal photomultipliers, IEEE J. Quantum Electron. 10 (8) (1974) 590–596, http://dx.doi.org/10.1109/JQE.1974.1068206.
[8] F. Hueso-González, D. Ginestar, J.L. Hueso, J. Riera, Comments on "SPICE model of photomultiplier tube under different bias conditions", IEEE Sens. J. 21 (15) (2021) 17395–17402, http://dx.doi.org/10.1109/JSEN.2021.3062428.
[9] D.Y. Akimov, E.S. Kozlova, Y.A. Melikyan, Computer modelling of the Hamamatsu R11410-20 PMT, J. Phys. Conf. Ser. 798 (2017) 012211, http://dx.doi.org/10.1088/1742-6596/778/1/012211.
[10] J. Peña-Rodríguez, S. Hernández-Barajas, Y. León-Carreño, L.A. Núñez, Modeling and simulation of the R5912 photomultiplier for the LAGO project, IEEE Sens. J. 21 (18) (2021) 20184–20191, http://dx.doi.org/10.1109/JSEN.2021.3096426.
[11] M. Heifets, P. Margulis, Fully active voltage divider for PMT photo-detector, in: IEEE Nucl. Sci. Symp. Conf. Rec., 2012, pp. 807–814, http://dx.doi.org/10.1109/NSSMIC.2012.6551216.
[12] E. Preziosi, A. Addis, C. Andreani, C. Cazzaniga, L. Fazi, C.D. Frost, M. Kastriotou, G. Levi, P. Picozza, V. Pietrosanti, G. Romanelli, M. Tardocchi, A. Ursi, E. Virgilli, R. Senesi, Effects of neutron irradiation on photomultiplier tubes and their power supplies, IEEE Trans. Nucl. Sci. (2023) 1, http://dx.doi.org/10.1109/TNS.2023.3309911.
[13] Y. Yu, H. Lv, K. Tariq, D. Liu, X. Sheng, C. Feng, Study of the performance of photomultiplier tubes at high variable counting rates, Nucl. Instrum. Methods Phys. Res. A 1008 (2021) 165433, http://dx.doi.org/10.1016/j.nima.2021.165433.
[14] K. Ackerstaff, J. Bisplinghoff, R. Bollmann, P. Cloth, F. Dohrmann, O. Diehl, G. Dorner, V. Drüke, H. Engelhardt, S. Eisenhardt, J. Ernst, P. Eversheim, D. Filges, S. Fritz, M. Gasthuber, R. Gebel, A. Gross, R. Gross-Hardt, F. Hinterberger, R. Jahn, U. Lahr, R. Langkau, G. Lippert, T. Mayer-Kuckuk, R. Maschuw, G. Mertler, B. Metsch, F. Mosel, H. Paetz gen. Schieck, H. Petry, D. Prasuhn, B. v. Przewoski, M. Radtke, H. Rohdjess, D. Rosendaal, P. von Rossen, H. Scheid, N. Schirm, F. Schwandt, W. Scobel, D. Theis, J. Weber, W. Wiedmann, K. Woller, R. Ziegler, Reduction of space charge effects and tests of larger samples of photomultipliers for the EDDA experiment, Nucl. Instr. Methods Phys. Res. A 335 (1) (1993) 113–120, http://dx.doi.org/10.1016/0168-9002(93)90262-G.
[15] H.J. Lush, Photomultiplier linearity, J. Sci. Instrum. 42 (8) (1965) 597–602, http://dx.doi.org/10.1088/0950-7671/42/8/328.
[16] P.L. Land, A discussion of the region of linear operation of photomultipliers, Rev. Sci. Instrum. 42 (4) (1971) 420–425, http://dx.doi.org/10.1063/1.1685117.
[17] Y. Zhu, S. Qian, Q. Wu, G. Zhang, L. Ma, Z. Wang, Study on fast timing MCP-PMT in magnetic fields from simulation and measurement, Sensors Actuators A 318 (2021) 112487, http://dx.doi.org/10.1016/j.sna.2020.112487.
[18] J. Beavers, K. Huddleston, N. Hines, W. McNeil, Modeling electron transport and multiplication in photomultiplier tubes using COMSOL Multiphysics®, J. Instrum. 17 (12) (2022) P12015, http://dx.doi.org/10.1088/1748-0221/17/12/P12015.
[19] L.W. Nagel, D. Pederson, SPICE (Simulation Program with Integrated Circuit Emphasis), Tech. Rep. UCB/ERL M382, EECS Department, University of California, Berkeley, 1973, URL http://www2.eecs.berkeley.edu/Pubs/TechRpts/1973/22871.html.
[20] G. Pausch, J. Berthold, W. Enghardt, K. Roemer, A. Straessner, A. Wagner, T. Werner, T. Koegler, Detection systems for range monitoring in proton therapy: Needs and challenges, Nucl. Instr. Methods Phys. Res. A 954 (2018) 161227, http://dx.doi.org/10.1016/j.nima.2018.09.062.
[21] F. Hueso-González, T. Bortfeld, Compact method for proton range verification based on coaxial prompt Gamma-ray monitoring: a theoretical study, IEEE TRPMS 4 (2) (2020) 170–183, http://dx.doi.org/10.1109/TRPMS.2019.2930362.
[22] B. Ripperda, F. Bacchini, J. Teunissen, C. Xia, O. Porth, L. Sironi, G. Lapenta, R. Keppens, A comprehensive comparison of relativistic particle integrators, Astrophys. J. Suppl. Ser. 235 (1) (2018) 21, http://dx.doi.org/10.3847/1538-4365/aab114.
[23] J. Boris, Relativistic plasma simulation-optimization of a hybrid code, in: Proc. Fourth Conf. Numerical Simulations of Plasmas (Washington, D.C.: Naval Research Laboratory), 1970, pp. 3–67, URL https://apps.dtic.mil/sti/citations/ADA023511.
[24] J. Vaughan, A new formula for secondary emission yield, IEEE Trans. Electron Devices 36 (9) (1989) 1963–1967, http://dx.doi.org/10.1109/16.34278.
[25] C. Vicente, M. Mattes, D. Wolk, B. Mottet, H. Hartnagel, J. Mosig, D. Raboso, Multipactor breakdown prediction in rectangular waveguide based components, in: IEEE MTT-S International Microwave Symposium Digest, 2005., 2005, pp. 1055–1058, http://dx.doi.org/10.1109/MWSYM.2005.1516852.
[26] A.H. Sommer, Bialkali (K_2CsSb) photocathode as a high-gain secondary electron emitter, J. Appl. Phys. 43 (5) (1972) 2479–2480, http://dx.doi.org/10.1063/1.1661537.
[27] D. González-Iglesias, Analysis of the multipactor effect in microwave waveguides and transmission lines (Ph.D. thesis), Universitat de València, 2017, URL https://roderic.uv.es/handle/10550/60416.
[28] R. Kikinis, S.D. Pieper, K.G. Vosburgh, 3D slicer: A platform for subject-specific image analysis, visualization, and clinical support, in: Intraoperative Imaging and Image-Guided Therapy, Springer New York, 2014, pp. 277–289, http://dx.doi.org/10.1007/978-1-4614-7657-3_19.
[29] S. Rit, M.V. Oliva, S. Brousmiche, R. Labarbe, D. Sarrut, G.C. Sharp, The reconstruction toolkit (RTK), an open-source cone-beam CT reconstruction toolkit based on the insight toolkit (ITK), J. Phys. Conf. Ser. 489 (1) (2014) 012079, http://dx.doi.org/10.1088/1742-6596/489/1/012079.
[30] MATLAB (R2022b), The MathWorks Inc., Natick, Massachusetts, 2022, URL https://es.mathworks.com/products/matlab.html.
[31] FreeCAD 0.20, 2022, URL https://www.freecad.org/index.php.
[32] J. Tuszynski, In_polyhedron, MATLAB Central File Exchange, 2023, URL https://es.mathworks.com/matlabcentral/fileexchange/48041-in_polyhedron.
[33] J. Greenwood, The correct and incorrect generation of a cosine distribution of scattered particles for Monte-Carlo modelling of vacuum systems, Vacuum 67 (2) (2002) 217–222, http://dx.doi.org/10.1016/S0042-207X(02)00173-2.
[34] K. Halbach, R.F. Holsinger, Superfish -a computer program for evaluation of RF cavities with cylindrical symmetry, Part. Accel. 7 (1976) 213–222, URL https://inspirehep.net/files/76ad49d27c8d9b6069ed25b6c67b44b0.
[35] D. Calvo, KM3NeT Collaboration, Nanobeacon: A low cost time calibration instrument for the KM3NeT neutrino telescope, AIP Conf. Proc. 1630 (1) (2014) 138–141, http://dx.doi.org/10.1063/1.4902791.
[36] COMSOL Multiphysics®(V5.6), COMSOL AB, Stockholm, Sweden, 2022, URL https://www.comsol.com.

Pablo Martín-Luna received the degree in physics and the master's degree in advanced physics from the University of Valencia, Valencia, Spain, in 2020 and 2021, respectively, where he is currently pursuing the Ph.D. in physics. His current research interests include numerical simulations of the relativistic dynamics of charged particles in electromagnetic fields and the study of novel particle acceleration techniques using carbon nanostructures.

Daniel Esperante is an applied scientist (Telecommunications Engineering and Ph.D. in Physics) with a large international experience in R&D in instrumentation for particle physics experiments and Radio-Frequency (RF) accelerators. He has played a leading role in the coordination, design, development and commissioning of scientific instrumentation and complex electronic systems at various particle physics experiments and accelerators facilities. Currently he is the scientific responsible of design and commissioning of the IFIC's high-gradient Radio-Frequency laboratory for medical accelerators and other applications.

Antonio Fernández Prieto holds a B.S. degree in Industrial Electronics from the University of León and a Ph.D. in Information Technology Research from the University of Santiago de Compostela. He is currently a researcher affiliated with the Galician Institute for High Energy Physics (IGFAE) and the European Organization for Nuclear Research (CERN). His main research interests include data acquisition systems, electronics design for photodetectors and silicon pixel detectors, as well as the integration of components within complex system architectures.

Nuria Fuster-Martínez received the Licenciado degree in physics, the master's degree in advanced physics and the Ph.D. in physics from the University of Valencia, Valencia, Spain, in 2011, 2012 and 2017, respectively. She has a large international experience in beam dynamics simulations of charged particle beams in accelerators; calculation of impedances and wakefields in accelerator structures; beam operation in linear and circular high-energy accelerators; and beam instrumentation R&D for linear colliders. Since 2020 she is focusing her research activities on accelerator applications in medicine, in particular, in high-gradient accelerators physics and technology and novel radio-therapy techniques.

Iris García Rivas is a Ph.D. student in Nuclear and Particle Physics. After finishing her studies in Physics with the specialization in Nuclear Physics, she started to work in the Galician Institute of High Energy Physics (and in collaboration with the Institute for Corpuscular Physics, Valencia) within the framework of the development of a novel detection system for proton therapy treatments monitoring. More recently, she started her Ph.D. program in the University of Santiago de Compostela in consortium with the company TripleAlpha Innovation to continue contributing to this promising project.

Benito Gimeno received the Licenciado degree in physics and the Ph.D. degree from the University of Valencia, Valencia, Spain, in 1987 and 1992, respectively. He became a Full Professor at the University of Valencia in 2010. His current research interests include the electromagnetic analysis and design of microwave passive components, RF breakdown high-power effects, particle accelerators for hadrontherapy, and dark matter axions search in the microwave frequency range.

Damián Ginestar earned his degree in Physics (1986) from Universitat de València (Spain) and his Ph.D. (1995) from the Universitat Politècnica de València (Spain). He works for the Applied Matematics Department at the Universitat Politècnica de València (Spain) as full professor of Applied Mathematics and he is a member of the Instituto Universitario de Matemática Multidisciplinar. His research interests are many devoted to develop scientific computation methods applied to engineering problems, mainly related with nuclear reactor physics. Also he has performed some studies related with water and nitrogen dynamics in soils and with digital video analysis.

Daniel González-Iglesias received the Licenciado degree in physics, the master's degree in advanced physics and the Ph.D. in physics from the University of Valencia, Valencia, Spain, in 2010, 2011 and 2017, respectively. His current research interests include theoretical analysis of high-power phenomena (RF breakdown, multipactor) in microwave passive components for space communications systems and for particle accelerators applications, and the design of RF electron photoinjector guns for x-ray free electron lasers (FEL).

José L. Hueso earned his M.Sc. (1976) and Ph.D. (1984) in Mathematics from the Universitat de València (Spain). He has worked from 1976 to 2016 at the Universitat Politècnica de València (Spain) as associate professor of Applied Mathematics and has been a member of the Instituto Universitario de Matemática Multidisciplinar. His research interests include locally convex spaces, parallel computation, systolic algorithms, optical flow, local and semilocal convergence and dynamics of iterative method for nonlinear equations and systems and its application to economical models, and video analysis and simulation of physical processes.

Gabriela Llosá has a Ph.D. in physics since 2005. She is a researcher at the Instituto de Física Corpuscular (IFIC), Valencia and the coordinator of the IRIS group (Image Reconstruction, Instrumentation and Simulations for medical imaging applications). She started her career in particle physics experiments and she has acquired a large international experience in detector development for medical applications. Her current research is focused on the development of medical imaging detectors and she is among the leading experts in Compton cameras. She is currently involved mainly in hadron therapy treatment monitoring and assessment of treatments with radiopharmaceuticals.

Pablo Martinez-Reviriego received the degree in physics from the University of Sevilla in 2019 and the master's degree in advanced physics from the University of Valencia in 2020, where he is currently pursuing the Ph.D. in physics. His current research interests include the studies of the viability of High-Gradient accelerator structures for their use in medical accelerators for hadrontherapy treatments in hospitals. In particular, he studies the non-linear phenomena such as RF breakdowns and dark currents, and their consequences in the accelerator cavities and their surroundings. Furthermore, he works on the RF design of Dielectric Loaded Accelerating structures for low beta particles.

Alba Meneses Felipe received Bachelor's in Biomedical Engineering from Polytechnic University of Valencia, Spain, in 2020 and Master's in Medical Physics from University of Valencia, Spain, in 2022. She is studying Ph.D. in Applied Medicine and Biomedicine at University of Navarra, Spain. Her research is focused on the evaluation of the absorbed dose in pencil beam scanning proton therapy treatments of tumors which exhibit respiratory motion.

Jaime Riera received his Ph.D. degree in Physics in 1990 from Universitat de València. He is a full professor in the Department of Applied Physics at the Universitat Politècnica de València (Spain). Dr. Riera has directed projects focused on the transmission of scientific knowledge through Information and Communication Technologies (ICTs). He has produced several documentaries on scientific subjects. He is currently researching at the Multidisciplinary Mathematics Institute, in the area of applications of image processing and digital tracking to medicine.

Pablo Vázquez Regueiro is Professor at U. Santiago de Compostela since 2013 with large background in particle detectors for High Energy Physics as the Silicon Tracker and the vertex detector for the LHCb experiment at CERN. He has expertise in silicon pixels, module production, quality assurance, electronics, detector commissioning or 4D tracking. Furthermore, he has produced a photodetector system based on APDs for quantum information processing and currently he is developing a new system for in vivo proton range verification with application in proton therapy treatments based on a scintillating crystal with a photomultiplier with active voltage divider and fast ADC.

Fernando Hueso-González did his Ph.D. on medical physics at Technische Universität Dresden thanks to a Marie Curie Early Stage Researcher fellowship, investigating on Compton cameras for proton therapy range verification. He then spent three years as a Postdoctoral Fellow at Harvard Medical School and Massachusetts General Hospital, working on the clinical translation of a collimated prompt gamma-ray camera from the lab bench to the proton treatment room. Currently, he is a Distinguished Researcher at IFIC leading a novel project on uncollimated prompt gamma-ray detection in a coaxial orientation.